2021 年臺灣國際科學展覽會 優勝作品專輯

作品編號 **100044**

參展科別 工程學

作品名稱 **Development of a rotor blade with optimized aerodynamics to propel a quadcopter**

得獎獎項 大會獎 三等獎
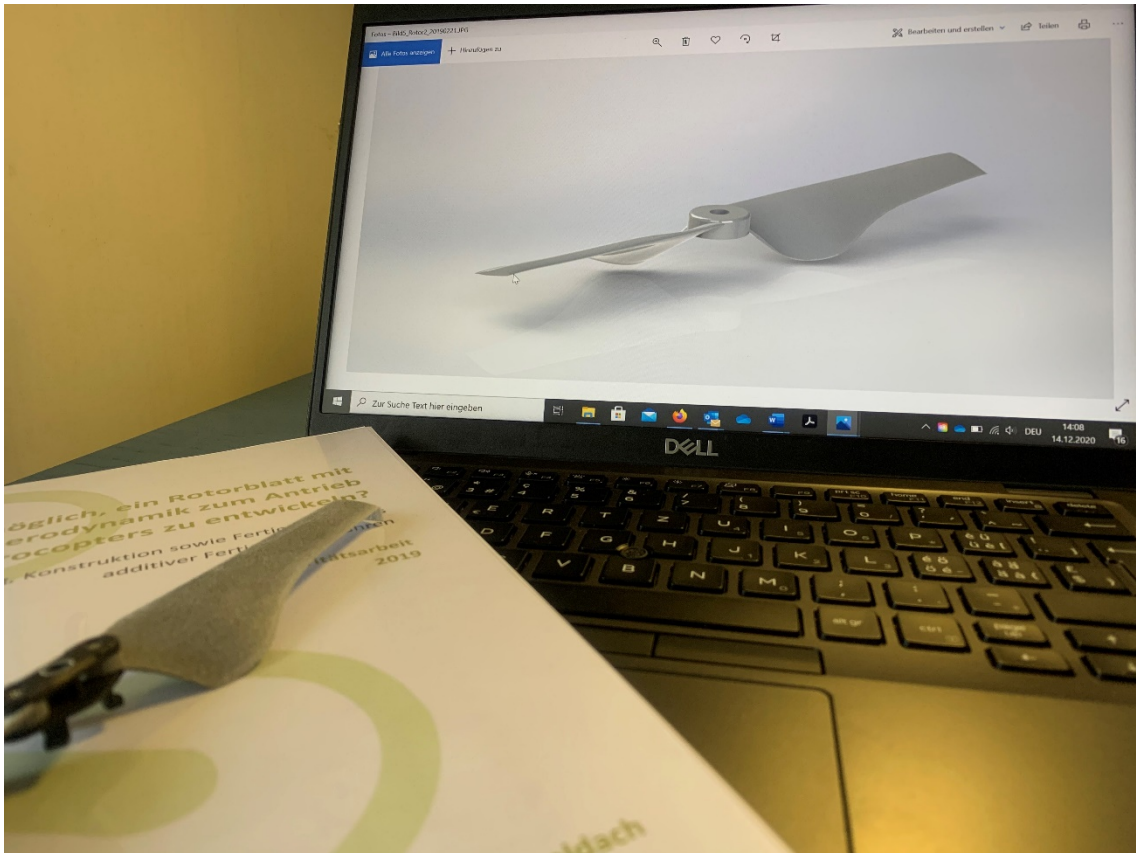
國　　家 **Switzerland**

就讀學校 **Freies Gymnasium Zürich**

指導教師 **Freies Gymnasium Zürich**

作者姓名 **Max Schaldach**

關鍵詞 **Fluid mechanics、aerodynamics、rotor blades**

作者照片

1. Introduction

Sustainable mobility concepts are playing an increasingly important part in today's social developments. As a promising mode of future transportation, quadcopters play a special role, and their further development and optimization is being advanced along many disciplines.

Even in my hometown of Zurich this trend has not passed by without leaving its marks. Since 2019, the Swiss National Postal Service has been testing autonomous means of transport together with the Zurich University Hospital as part of a pilot project. However, quadcopters are not exclusively used for transportation purposes. Geologists use them for landscape modeling and the insurance industry utilizes them for damage assessment. Quadcopters have also become an integral part of photography and agriculture, where they are used for pest control, for example [2].

I first became intensively involved with quadcopters in 2017, when I received a hobby model for my birthday in the form of the Mavic Pro from the Chinese company Da-Jiang Innovations Science and Technology Co., Ltd (DJI). In October of the same year, I completed an internship in the biofluid mechanics department of the Institute for ImplantTechnology and Biomaterials e.V., where I studied the aerodynamics of airfoils. With my Mavic Pro in my backpack, I had the idea to develop and prototype my own functional rotor for my quadcopter as part of my upcoming Swiss Matura thesis paper. The rotor would be considered functional if it generates enough lift to keep the quadcopter hovering. The focus of this project was the investigation of aerodynamic properties. The influence of other factors, such as the material used, was not the primary focus of the work and therefore not investigated in detail.

2. Theoretical principles

2.1. Structure of a rotor

A rotor is a rotating wing. In the application field of quadcopters, a rotor usually consists of two rotor blades. With their blade roots - the outer edge of a rotor blade - they are attached to a connection piece, around which they rotate. The length of a rotor blade is defined as the distance from the connection piece to the blade tip, which is half the diameter of the rotor. The "width" of the rotor blade is defined as the *airfoil depth*.
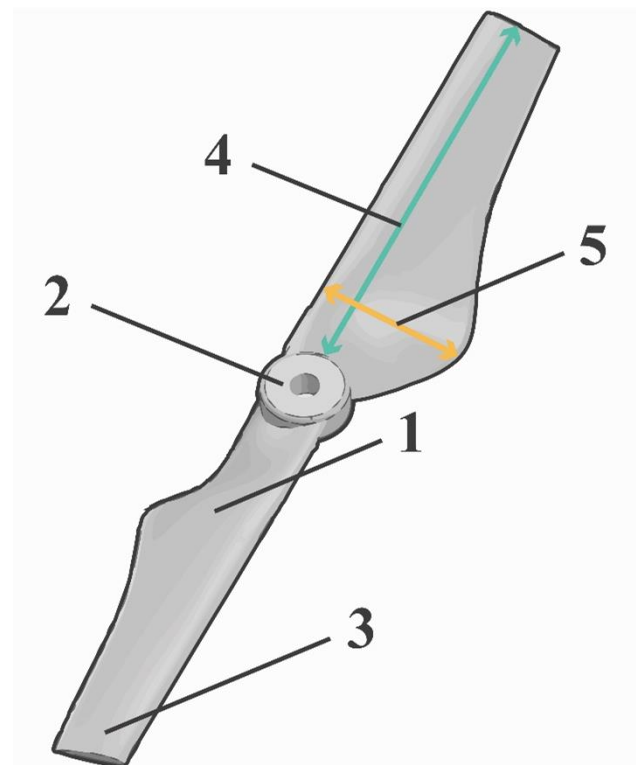

Figure 1: Structure of a rotor 1. Blade root 2. Connection piece 3. Blade tip 4. Blade length 5. Airfoil depth

The basic structure of a rotor blade is formed by so-called airfoils: These are cross-sections through a rotor. They can be described geometrically using coordinates in the xy plane; at a later stage, these are used to calculate and design the rotor. Depending on what rotors are used for, their airfoils have different shapes. The determination of their ideal shape is achieved with methods as the Kutta-Schukowski transformation [1].
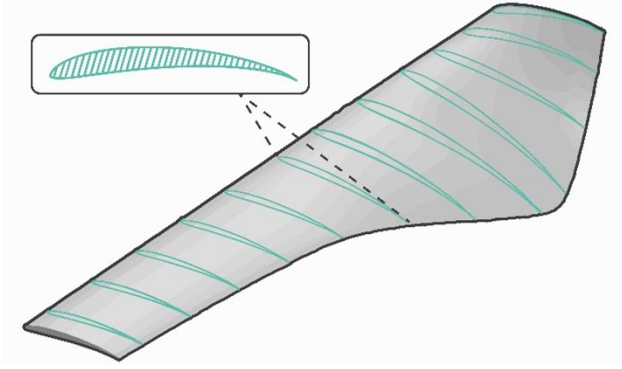
Figure 2: Visualization of the airfoil skeleton of a rotor blade

2.2. Dynamic lift force

There are two main forces acting on a rotor as air flows around it. One of them is the dynamic lift force, whose occurrence is described by the Bernoulli equation [3]. When transforming the basic equation, it becomes apparent that a change in velocity Δu results in a change in pressure Δp. Areas with high flow velocities have a lower air pressure than areas with low flow velocities. Due to the unequal velocities on the upper and lower side of the rotor, an area of low pressure is formed on the upper side and an area of high pressure on the lower side of the rotor. This pressure difference leads to the occurrence of the dynamic lift force.
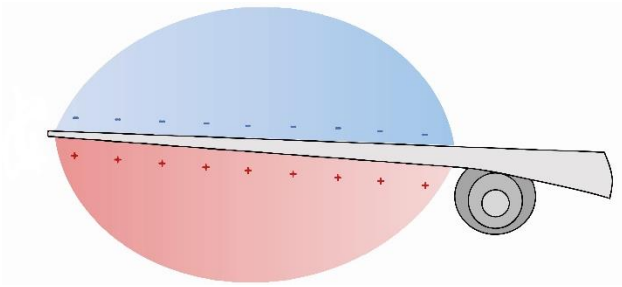

Figure 3: Conceptual representation of the low-pressure (blue) and high-pressure (red) regions on an aircraft wing

$$F_L = \frac{1}{2} * \rho * w^2 * c_L * A \qquad (1)$$

The lift equation contains four variables: the air density ρ, the *effective inflow velocity* w, the *lift coefficient* c_L, and the *lift-effective area* A. According to the laws of Betz and Schmitz an ideal rotor will have a homogeneous distribution of the lift force acting on it [4]. However, due to the effective inflow velocity w, which increases from the blade root to the blade tip, the distribution is non-uniform. Due to the quadratic influence of the effective inflow velocity on the lift force (cf. equation 1), enormous lift forces can be induced at the blade tip. Towards the blade root, the lift force decreases exponentially until it reaches a value of $F_L = 0$ N at the connection piece. This uneven distribution of the lift force leads to aerodynamic disadvantages [4]. By varying the airfoils and thus the lift coefficient c_L as well as adjusting the lift effective area A, an approximation to a uniform distribution of the lift force can be achieved. This is the basic idea on which the modification of the rotor in this paper is built upon.

2.3. Drag force

The second significant force acting on a rotor is air resistance. When a rotor moves through a fluid, gas molecules continuously collide with its surface. This force effect is also referred to as *active drag* [5]. The larger the frontal area of a rotor, the higher the drag.

$$F_D = \frac{1}{2} * \rho * w^2 * c_D * A_c \qquad (2)$$

Like the lift force, the active drag force F_D is dependent on the air density ρ and the effective inflow velocity w. Furthermore, it relates to the cross-sectional area A_c and the *drag coefficient* c_D.

In addition to the active drag, the movement of the rotor causes *induced drag* [6]. Due to the different pressure areas on the upper and lower side of a rotor, the air will attempt to flow around the tip of the blade. These air currents are known as *crosscurrents*. Since the rotor moves forward simultaneously with the lateral flow around it, some air flowing upward is entrained, and edge turbulences form, slowing down the rotor. By adding winglets, the occurrence of these vortices can be prevented [7]. The winglets on quadcopters, helicopters, and wind turbines are usually bent towards the lower side of the blade, unlike on airplanes. As a result, the air is prevented from flowing around the rotor tip. The pressure gradient is maintained to a greater extent, resulting in a higher lift force ($\Delta p \propto F_A$) and the formation of the edge vortices is reduced, causing less induced drag.
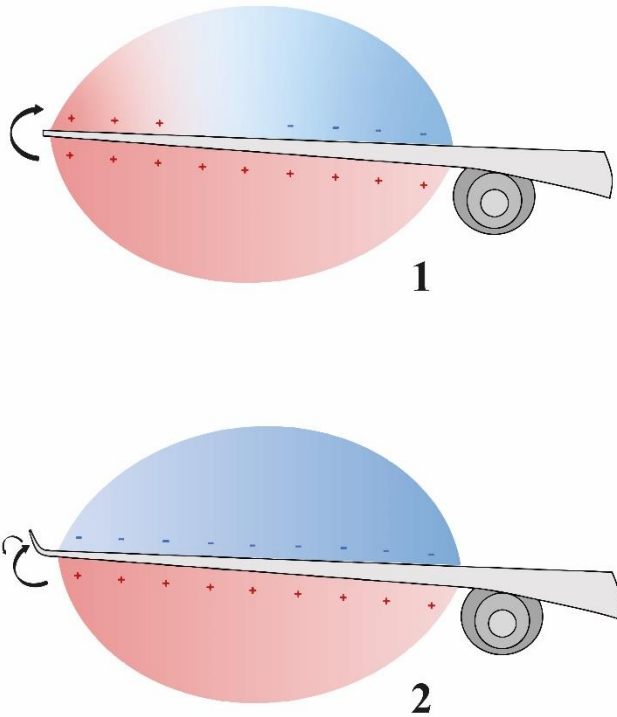
Figure 4: 1. Effects of crosscurrents on the two different pressure regions 2. Prevention of crosscurrents by using winglets

3. Calculation of the rotor

The *Propeller Theory by Betz and Schmitz* [4] served as the basis for the calculation of the rotors. It contains equations and calculation rules which enable to design rotors on the basis of aerodynamic laws and is mainly used for the design of wind turbines.

3.1. Airfoil selection

The first step was the selection of suited airfoils. The publicly accessible website Airfoils.de [8] provides a database containing a total of 1,636 airfoils together with their aerodynamic characteristics. Of particular interest are the lift coefficient c_L and the drag coefficient c_D. They are characteristic parameters for describing the lift and drag behavior of an airfoil. The larger the lift coefficient of an airfoil, the more lift the rotor generates. Conversely, the smaller the drag coefficient, the less active drag is generated at the rotor. It is therefore of interest to install airfoils with high lift coefficients and low drag coefficients.

For the first prototype (*Design I*), the ONERA OA209 airfoil was selected. It is typically used for man-carrying helicopters whose rotors have similar flow characteristics as the rotors of a quadcopter. Due to a lack of test results, it was assumed that the airfoil would also be suitable for use on the Mavic Pro. ONERA OA209's lift coefficient of $c_L = 0.7$ falls in the middle range compared to other airfoils [8]. As for the drag coefficient of $c_D = 0.03$, it is comparatively low [8].

In order to achieve a more even distribution of the lift force than with *Design I*, it was decided to use two airfoils for the second prototype (*Design II*). Airfoils with high lift coefficients are used at the blade root. The airfoils in the direction of the blade tip have decreasing lift coefficients. For the area of the blade root, the AH-7-47-6 airfoil was selected, which has a c_L value of 1.6 and a c_D value of 0.06 [8]. Preceding calculations revealed that the lift coefficients of the two airfoils must have a minimum difference of 0.3 to approximate a more uniform distribution of the lift force. Using airfoils with lower lift coefficients may result in a more homogeneous lift distribution, but the rotor also generates less lift. Therefore, the E71 airfoil with a c_L value of 1.3 and a c_D value of 0.07 seemed particularly suitable for the blade tip area [8].
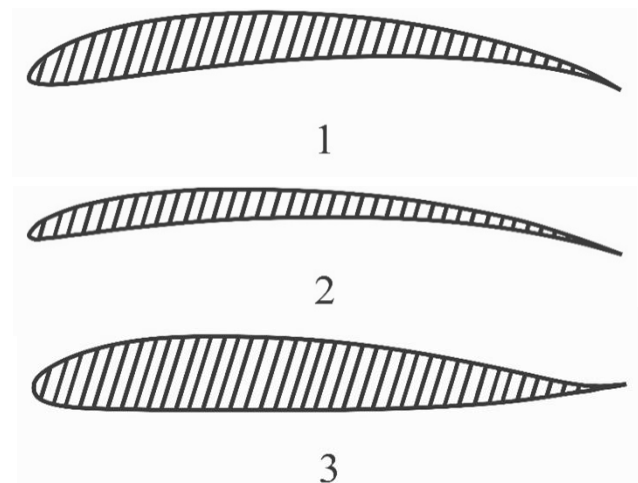

Figure 5: Side view of the airfoils used for *Design II* and *Design I* 1. AH-7-47-6 airfoil 2. E71 airfoil 3. ONERA OA209 airfoil

Table 1: Comparison of the lift coefficients of different airfoils available on Airfoils.de

Lift coefficients (c_L)	$c_L > 1,5$	$1,2 < c_L < 1,5$	$c_L < 1,2$
Airfoil (c_L)	**AH-7-47-6 (1,6)**	AH-6-40-7 (1,5)	BL145 (1,1)
	E61 (1,6)	E385 (1,5)	SD7090 (1,1)
	cp-160-050-gn (1,6)	AH 79-100 A (1,4)	HQ 1.0/10 (0,9)
	AH 79-100 B (1,6)	BE50 (1,3)	NACA 5-H-10 (1,0)
	FX 63-120 (1,6)	**E71 (1,3)**	NACA 63-210 (1,0)

With an overall length of the rotor of 10.5 cm, its basic skeleton is composed of eleven support points, for each of which a suitable airfoil was scaled. Except for the last airfoil, these follow each other at regular intervals of one centimeter.

3.1.1. Reynolds number

The *Reynolds number* R_e is a dimensionless parameter that describes whether a flow is laminar or turbulent. The Reynolds number is determined using equation 3.

$$R_e = \frac{L*w}{v} \qquad (3)$$

It is dependent on the airfoil depth L, the effective flow velocity w, and the kinematic viscosity v. The latter is a temperature-dependent constant that describes the viscosity of a fluid. Under normal conditions, its value is $15.2 * 10^{-6} \frac{m^2}{s}$. For the blade tip, the Reynolds number was $R_e = 38.600$ and for the blade root, $R_e = 6.400$. Thus, the degree of turbulence of the airflow at the blade tip is presumably greater than at the blade root. Depending on the Reynolds number, the aerodynamic coefficients of an airfoil vary. Since only airfoil coefficients for Reynolds numbers of $R_e > 50.000$ were available on Airfoils.de, these coefficients had to be used for the subsequent calculations.

3.2. Modification of the airfoils

Following the airfoil selection, the airfoil coordinates were modified with two parameters. The *airfoil depth* was used to stretch airfoils horizontally in relation to their distance from the blade root to achieve a more homogeneous distribution of the lift force generated by the rotor. As a result, the airfoil depth decreased from the blade root to the blade tip. The *construction angle* was used to align the airfoils parallel to the airflow direction - depending on their distance from the blade root [4]. Airfoils at the blade root were tilted more than at the blade tip.

3.2.1. Airfoil depth

The *airfoil depth L* is a partial value of the lift-effective area A and describes the length of an airfoil. It is a component of the lift force equation.

$$F_L = \frac{1}{2} * \rho * w^2 * c_L * L * B \qquad (4)$$

The density of the air ρ, the lift coefficient c_L and the constant B are known. The effective flow velocity w is composed of two partial velocities: The vertical velocity v_D and the circumferential velocity u_r. These can be determined with the help of anemometers and equations included in the *Propeller Theory by Betz and Schmitz*. Unlike v_D, which describes the velocity of the vertical airflow and was measured using an anemometer, u_r is the velocity of the rotor, which is different at each point of the rotor blade due to its rotational motion. Since the circumferential velocity is related to the radius (cf. equation 5), it increases with the distance from the blade root of the blade tip. This results in different effective flow velocities for each airfoil on the rotor blade.
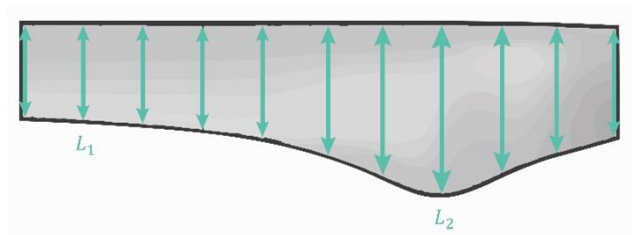

Figure 6: Effect of airfoil depth ($L_2 > L_1$) on a rotor blade from top view

$$u_r = r * 2 * \pi * n \qquad (5)$$

To calculate the reference value of the lift force, an airfoil depth of 1.5cm was defined for the blade tip. Measurements had shown that a rotor up to a blade tip depth of 1.5cm fits on the fixtures of the Mavic Pro. This resulted in a lift force of 0.133N for the most outer area of the rotor. To calculate the airfoil depths for the individual airfoils, the equation of the lift force was then transformed (cf. equation 6).

$$L = \frac{2 * F_A}{\rho * w^2 * c_A * B} \qquad (6)$$

For each airfoil of the rotor, the equation resulted in different airfoil depths. Due to the quadratic influence of the effective inflow velocities, the airfoil depths at the blade root turned out to be so large that they could not be technically realized. In the case of a rotor with a homogenous lift distribution, an airfoil at the blade root is 250 times as long as at the blade tip. Figure 7 illustrates this extreme difference in airfoil depth.
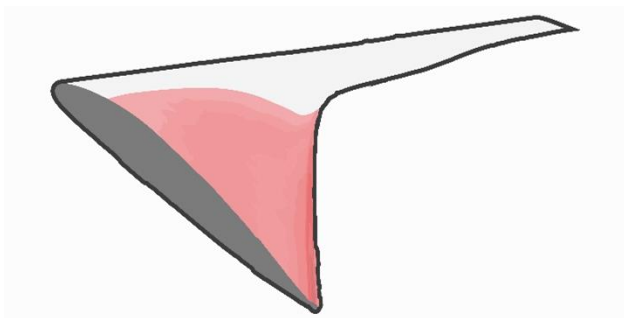

Figure 7: Illustration of an "ideal rotor". Reference is made to the high airfoil depths in the area of the blade root (colored red), which are technically impossible to realize.

Consequently, it was necessary to undertake deviations from the ideal state of a rotor blade, which resulted in an approximation of a uniform distribution of the lift force. In order to avoid making these deviations arbitrarily, existing quadcopter rotors served as templates. Similarly to the airfoil selection, the lessons learned from *Design I* with regard to the airfoil depth were implemented into *Design II*. When compared to *Design I*, the airfoils at the blade root

of *Design II* were stretched to a greater extent than at the blade tip.

After completing these calculations, the airfoil coordinates were multiplied by the obtained values.

$$x` = x * L \qquad (7)$$

$$y` = y * L \qquad (8)$$

Table 2: Airfoil depths obtained for *Design I*

Airfoil	r (in m)	L (in m)
Blade root (ONERA OA209)	0	0,02
	0,01	0,0165
	0,02	0,025
	0,03	0,03
	0,04	0,027
	0,05	0,0225
Blade tip (ONERA OA209)	0,06	0,02
	0,07	0,0185
	0,08	0,0175
	0,09	0,0165
	0,1	0,0155
	0,105	0,015

Table 3: Airfoil depths obtained for *Design II*

Airfoil	r (in m)	L (in m)
Blade root (AH-7-47-6)	0	0,02
	0,01	0,0215
	0,02	0,026
	0,03	0,028
	0,04	0,0245
	0,05	0,021
Blade tip (E71)	0,06	0,019
	0,07	0,0175
	0,08	0,0165
	0,09	0,0158
	0,1	0,01525
	0,105	0,015

3.2.2. Construction angle

The unequal effective inflow velocities also result in different inflow directions for the individual support points

of the rotor blade. At the blade tip, the airflow is almost horizontal due to the high circumferential velocities. In the case of airfoils at the blade root, on the other hand, the air meets the rotor from almost vertically.
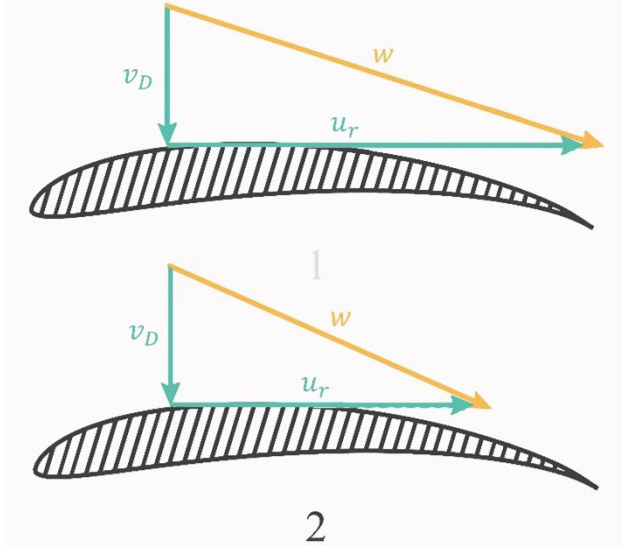

Figure 8: Illustration of the effective inflow velocity w with velocity triangles at two positions of a rotor blade (circumferential velocity u_r, vertical velocity v_D). The higher circumferential velocity at airfoil 1 (blade tip) leads to a more horizontal incident flow than at airfoil 2 (blade root).

The aim of the *construction angle* α_K is to align the airfoils locally, i.e. as a function of the vector of the effective flow velocity, parallel to the airflow.
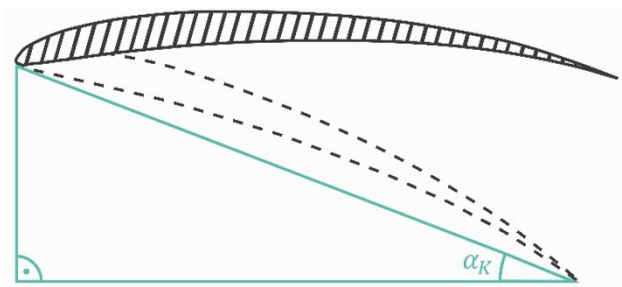

Figure 9: Airfoils are aligned parallel to the airflow with the aid of the construction angle

$$\alpha_K = \alpha_A + \alpha_E \qquad (9)$$

The construction angle is composed of the *angle of attack* α_A and the *incidence angle* α_E [4]. The determination of the angle of attack is directly related to the airfoil selection through the lift coefficient c_L. The relationship of the lift coefficient to the angle of attack is the same for all similar airfoils and can be derived from airfoil plots (see Figure 10). The larger the value of the angle of attack, the higher the lift coefficient. However, if the value of the angle of attack is set too high, a stall may occur [9] and the rotor will no longer generate lift. This point is marked by a bend in the airfoil plot.
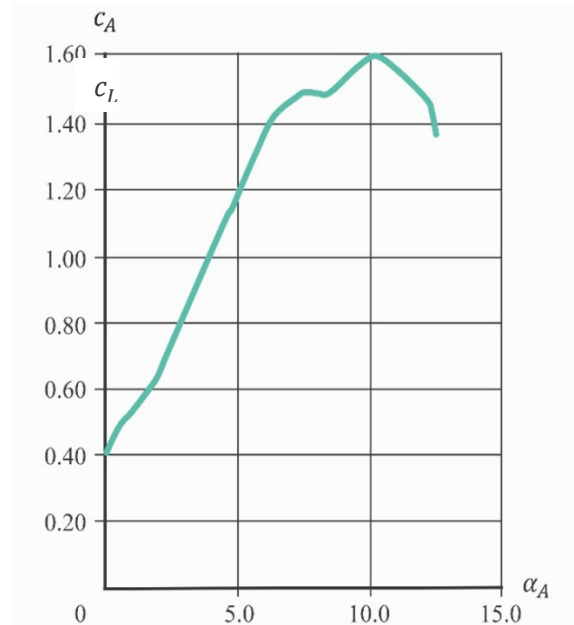

Figure 10: Relationship between angle of attack (x-axis) and lift coefficient (y-axis) for the AH-7-47-6 airfoil

To counteract this risk, the angles of attack were selected below the critical stall point. For the ONERA OA209 airfoil of *Design I*, the value was 5º. For *Design II*, the value was 5º for the E71 airfoil and 8º for the AH-7-47-6 airfoil.

$$\alpha_E = arctan\left(\frac{2}{3} * \frac{R}{r * \lambda_i}\right) \quad (10)$$

The *incidence angle* α_E had to be determined for each airfoil of the eleven support points via equation 9. The distance of an airfoil from the blade root is described by the variable r. The total length of the rotor R is constant. Another constant is the so-called *induced flow rate* λ_i, which is calculated from the ratio of the circumferential velocity at the tip of the rotor to the vertical velocity. Among other factors, it is dependent on the rotational frequency n.

5

After calculating the construction angles for the eleven support airfoils, the airfoil coordinates were modified using equations 11 and 12.

$$x`` = x` * cos(\alpha_K) - y` * sin(\alpha_K) \qquad (11)$$

$$y`` = x` * sin(\alpha_K) + y` * cos(\alpha_K) \qquad (12)$$

Table 4: Construction angles obtained for *Design I*

Airfoil	r (in m)	α_K
Blade root (ONERA OA209)	0	0°
	0,01	-59,2°
	0,02	-47,8°
	0,03	-39,8°
	0,04	-34,1°
	0,05	-29,8°
Blade tip (ONERA OA209)	0,06	-20,5°
	0,07	-19,2°
	0,08	-18,0°
	0,09	-17,1°
	0,1	-16,2°
	0,105	-15,5°

Table 5: Construction angles obtained for *Design II*

Airfoil	r (in m)	α_K
Blade root (AH-7-47-6)	0	0°
	0,01	-45,0°
	0,02	-28,6°
	0,03	-22,1°
	0,04	-18,7°
	0,05	-16,6°
Blade tip (E71)	0,06	-12,1°
	0,07	-11,1°
	0,08	-10,4°
	0,09	-9,78°
	0,1	-9,30°
	0,105	-9,10°

3.3. Design in SolidWorks and attachment of winglets

After the modification of the airfoil coordinates, they were formed into a 3D object with the CAD software SolidWorks. For this purpose, the modified airfoil coordinates were converted into text files, which could then be exported to SolidWorks. Since the program independently assembles the coordinate points into airfoils, these only had to be connected manually using a sketch function.

The final step of the construction of *Design I* was to design a connection piece with which the rotor could be attached to the quadcopter. The various sketch functions were used for this purpose.

In case of *Design II*, Winglets were additionally attached. Their areas of application are diverse and range from aircraft wings to wind turbine rotors. Since the winglets of wind turbines show greater similarities to the flow behavior of the rotors of a quadcopter than, for example, aircraft wings, they primarily served as a template [10]. There are no common calculation methods for winglets, which is why they had to be shaped manually in three dimensions using the sketch functions already mentioned. The shapes of the winglets were created using the spline function. A total of three different winglet variants were conceptualized and produced.

The idea behind the *circular* and *oval winglets* was to prevent or at least reduce the lateral crosscurrents. The development of the novel *sloped winglets* was much more complicated. Compared to the first two winglet variants, they have a decisive advantage: the downward-curved shape does not only prevent the air from flowing around the blade tips, but also deflects it specifically towards the ground. A downward air movement represents momentum. Based on the law of conservation of momentum, a counter momentum must exist [11]. This counter-momentum is the lift force. With the sloped winglets the rotor theoretically causes less drag on the one hand, and on the other hand it generates more lift. This is not the case with the other winglet variants: Due to their right-angled ascent, they solely serve as a barrier for the blade tip crosscurrents, thereby reducing the induced drag, but not generating any additional lift.
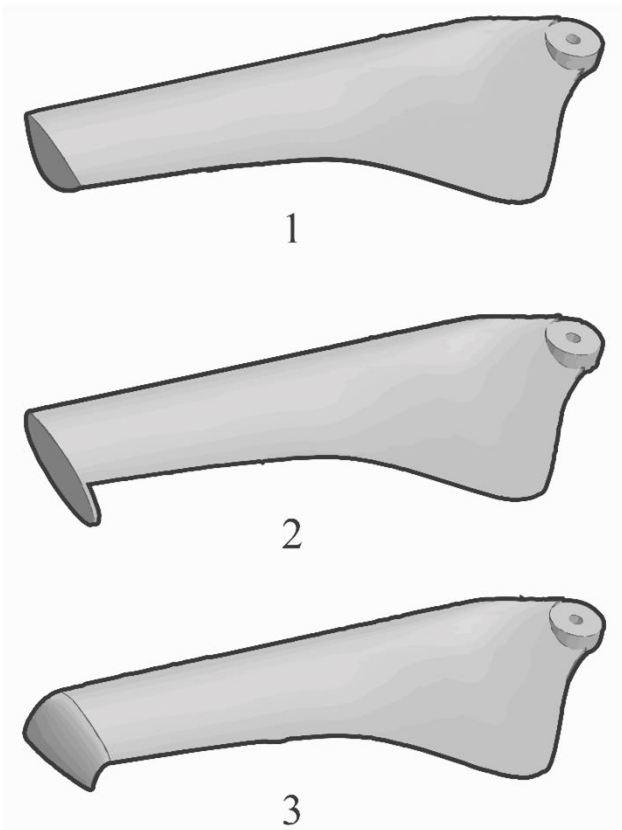
Figure 11: Winglet variants on *Design II* 1. Circular winglets 2. Oval winglets 3. Sloped winglets

3.4. Mechanical manufacturing

After completing the design process in SolidWorks, the rotors were 3D printed. For this purpose, the finished SolidWorks files were exported into the software of the 3D printer. The 3D printing process used is called *Polyjet*. The structures are applied layer by layer by curing liquid material with UV light.

Figure 12: *Design I* after completion of the 3D printing process

Figure 12 shows that the rotor was initially unusually thick. This is due to the fact that the 3D printer applies the material of the rotor onto so-called supporting structures. This layer was soft enough to be removed with a scalpel and a water jet. Finally, the printed prototypes were attached to the quadcopter with their connection piece. The final products are shown in figures 14 and 15.

Figure 13: Standard rotors of the Mavic Pro (DJI)

Figure 14: *Design I* with connection piece for test rig

Figure 15: *Design II* with sloped winglets

A second series of *Design II with sloped winglets* prototypes was printed for the test flights. For logistical reasons, this had to be done using a different 3D printer that works using a stereolithography process. Similar to the *Polyjet* process, a liquid material is cured by using UV light. However, this printing process requires a solid support structure to be built upon, which then had to be removed mechanically. This meant that the lower side of the rotor ultimately had a smoother surface than the upper side. The effects of this circumstance and the use of different materials allowed some conclusions to be drawn, which are described in Chapter 5.2.

4. Experiments

4.1. Measurements on the test rig

All 5 prototypes were compared to the DJI-standard rotors of the Mavic Pro on a stationary test rig. Furthermore, a comparison of the different winglet prototypes was conducted.

In order to determine the aerodynamic characteristics of the rotors, they were attached to a crossbeam with a motor. This structure was then positioned on a scale. When the rotor started turning, the scale indicated a lower weight due to the occurrence of the lift force. The magnitude of the lift force could be derived from the weight difference, since according to the principle of Newton's third law (for every action, there is an equal and opposite reaction) the lift force can be set equal to the gravitational force.

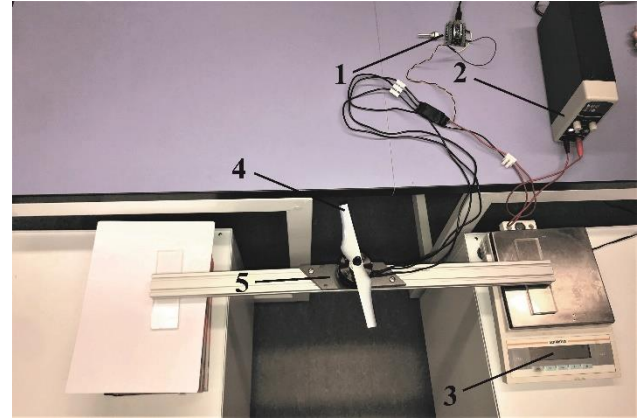$$F_A = 2 * \Delta F_G = 2 * \Delta m * g \qquad (13)$$

Figure 16: Setup of the test rig for determining the aerodynamic properties of the rotors 1. Controller 2. Power supply 3. Scale 4. Rotor 5. Motor

4.2. Test flights

After the experiments on the test rig, the DJI-standard rotors and *Design II* with sloped winglets were tested outdoors and compared with each other. A total of three test flights were conducted. The first was intended to determine whether the rotors would withstand the outdoor conditions. The second and third test flights were carried out to verify the results of the test rig, to answer questions about material aspects and to draw conclusions about the flight duration.

5. Results and discussion

5.1. Evaluation of the results of the test rig

5.1.1. Comparison of the *DJI-standard rotors* with *Design I* and *Design II*

In theory, the Mavic Pro takes off as soon as the rotor generates a lift force of 1.78 newtons. A stroboscope was used to determine the rotational rate at which the rotor generates this critical magnitude of lift force. This rate was defined as the critical rotational rate. From *Design I* to *Design II*, a significant difference could be observed. *Design II* required 6,100 rpm to get the Mavic Pro to hover, while *Design I* required 6,800 rpm. This improvement is subject to several factors: Starting with the airfoil selection, to the airfoil depth calculation, and the design steps in SolidWorks, significant deviations from *Design I* to *Design II* were made. During the process of *Design I*, the influence of the airfoil characteristics on a uniform lift

force distribution was significantly underestimated. With a specially created criteria catalog based upon the results from *Design I*, suitable profiles for *Design II* were filtered out separately for the blade root and blade tip areas. The subsequent modification of their airfoil coordinates with the airfoil depth was also a decisive factor for the improvement. In order to technically realize the rotor, strong deviations from the calculated values had to be undertaken. In the case of *Design II*, these deviations were deliberately kept small at the blade root; this allowed the resulting aerodynamic disadvantages to be minimized. Furthermore, minor changes in the determination of the angle of attack and the design process in SolidWorks contributed to the performance improvement from *Design I* to *Design II*. As a result of these changes, *Design II* achieved a more even distribution of the lift force and generated more lift than its predecessor.

However, both rotor designs performed worse than the DJI-standard rotors. These generate the critical magnitude of lift force at a rotational rate of 5,600 rpm.
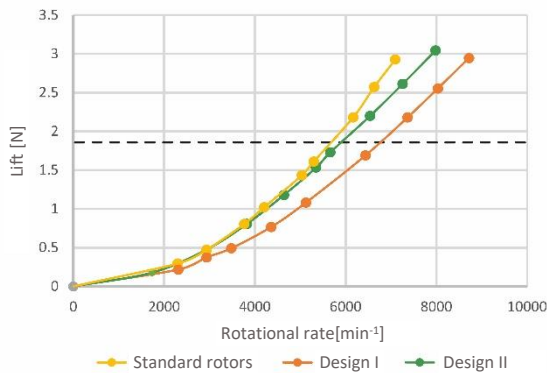

Figure 17: Comparison of *Design I*, *Design II* and the DJI-standard rotors in terms of their lift performance

5.1.2. Comparison of the winglet variants

By adding winglets to *Design II*, the aim was to achieve another approximation to the DJI-standard rotors. However, neither the circular nor the oval winglet made a decisive difference. From 6,100 rpm, which *Design II* without winglets needed for takeoff, a slight improvement of the critical rotational rate to 5,900 rpm was achieved for both variants. Thus, special attention was paid to the sloped

winglets. The rotational rate required for takeoff was 5,400 rpm. This not only makes it the most efficient of the three winglet variants, but also outperforms the DJI standard rotors by 200 rpm. The reason for this 700 rpm increase is the special form factor of the winglets. The considerations made in theory proved to be tenable.
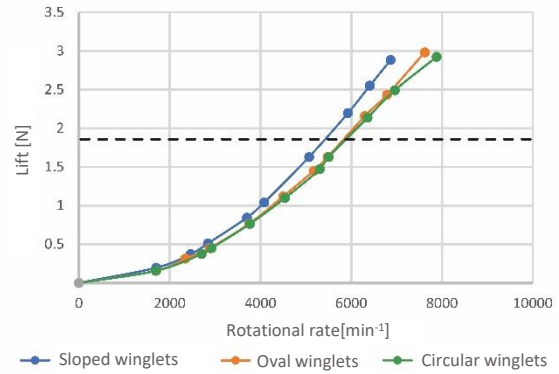

Figure 18: Comparison of circular, oval, and sloped winglets with regard to their lift performance
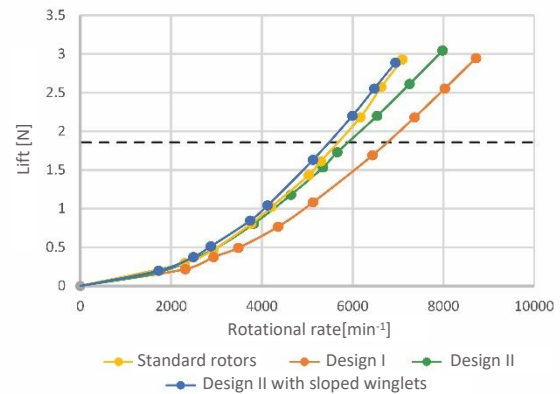

Figure 19: Comparison of *Design I*, *Design II*, *Design II* with sloped winglets and the DJI standard rotors in terms of their lift performance

5.2. Evaluation of the test flights

5.2.1. Aerodynamic findings from the test flights

The first test flight was to provide information on whether *Design II* with sloped winglets would withstand outdoor conditions. Although the test conditions were almost the same as on the test rig, material failure was more likely due to the high acceleration rates. The Mavic Pro was able to lift off and maintain its hover flight; thus, the initial objective of the project was met.

The second test flight built upon these findings and enabled a direct comparison of *Design II* with sloped winglets to the DJI-standard rotors under realistic conditions. To determine the aerodynamic characteristics of the rotors, their rotational speed could be read on the remote-control display. The critical rotational rate was used as the comparative criterion. The two rotors performed better under real conditions than on the test rig. With close to 4,800 rpm, *Design II* with sloped winglets once again outperformed the DJI-standard rotors (5,500 rpm). The difference to the test rig was the result of a conceptual design flaw. The crossbeam on which the motor was mounted, hindered the vertical acceleration of the air through the rotor, resulting in the need for a higher rotational rate to achieve the same lift.

Prior to the third test flight, the rotors were printed a second time. The removal of the solid support structures mentioned in chapter 3.4. resulted in an increased surface roughness of the upper side of the rotor. This caused *Design II* with sloped winglets to have higher rotational rates than during the second test flight: the critical value increased from 4,800 to 5,400 revolutions per minute. By making the top surface rougher than the bottom surface, the air pressure gradient between the upper and lower sides of the rotor was reduced. The smaller pressure gradient ultimately resulted in less lift being generated.

5.2.2. Electrodynamic findings from the test flights

The third test flight provided important insights into the electrodynamic performance of the rotors. Until the accumulator was fully discharged, the standard rotors were able to keep the Mavic Pro hovering for 23 minutes and 46 seconds. For *Design II* with sloped winglets, the flight time was 22 minutes and 15 seconds. Together with the *nominal power* of the accumulators, which amounted to 43.6Wh (=156,960Ws), it was possible to infer the electrical power. This was 110 watts for the DJI-standard rotors and 118 watts for *Design II* with sloped winglets. Consequently, more energy has to be supplied to the custom-designed

rotors than to the standard rotors over a certain period of time. Their energy efficiency is thus lower.

If these results are put in relation to those from the test rig, an interesting observation can be made. Although *Design II* with sloped winglets had generated more lift force on the test rig than DJI's-standard rotors, less energy had to be supplied to the latter.

5.2.3. Deviation between aerodynamic and electrodynamic results

Throughout the test flights, it was observed that the Mavic Pro compensated smallest gusts and unbalanced movements of its four rotors with the help of its sensor system. Using *Design II with sloped winglets*, these compensating movements were particularly strongly. Based on these observations, it was assumed that this had led to a faster discharge of the accumulators.

While it might well be that more energy was consumed by stronger sensor interventions, the shorter flight time could also have been caused by an aerodynamically less efficient rotor. The fact that a rotor delivers more lift at the same rotational rate is not the sole determinant of higher aerodynamic efficiency. Rotors whose airfoils have lower glide ratios (ratio between c_D and c_L) have a higher energy consumption. They produce the same lift at the same speed, but require more torque and therefore more power. In order to assess the efficiency of the tested rotors, the torque or the electrical input power of the motor would have had to be measured on the test rig. However, due to a lack of experimental equipment, it was not possible to determine these decisive characteristic values.

5.2.4. Insights into material issues

The manufacturing process can significantly affect the performance of the rotor. In the case of *Design II*, small printing errors, such as the increased surface roughness of the upper surface, led to a reduction in the pressure gradient and thus to a reduction in the lift force. The instability of the rotors observed during the third test flight allowed conclusions to be drawn about the suitability of the manufacturing process used to produce rotor blades.

Unlike standard commercial rotors, the rotor prototypes were manufactured using additive 3D printing. The material is applied layer by layer in a horizontal direction and then cured with UV light. This process is particularly suitable for the production of prototypes in small series. It is suspected that the layered structure of the used 3D printing process caused the rotor to flex more in flight than a standard rotor, which leads to aerodynamic disadvantages. This needs to be investigated further.

6. Summary

The objective of the paper was to design and manufacture a rotor that would allow the Mavic Pro quadcopter to achieve hover flight. The calculation of the rotor was based on the laws and equations of the *Propeller Theory by Betz and Schmitz*. A total of five different rotor designs were created.

The first design step was the selection of suitable airfoils. Then the airfoils were modified with two parameters: the airfoil depth and the construction angle. After their modification, the airfoil coordinates were formed into a 3D model using the CAD software SolidWorks. *Design II* also involved the addition of custom-designed winglets. Using additive manufacturing techniques, the rotors were then printed and compared on a stationary rotor test rig. The rotational rate at which the quadcopter theoretically starts to hover was used as a criterion for the aerodynamic performance of the rotors. This rate was defined as the critical rotational rate. The corresponding critical magnitude of lift force was determined with the aid of a laboratory scale.

To get the Mavic Pro to take off, *Design I* had to rotate at 6,800 rpm, while *Design II* only required 6,100 rpm. Both rotor designs needed a higher rotational rate than the DJI-standard rotors with 5,600 rpm. By adding the novel, self-designed *sloped winglets*, the Mavic Pro's standard rotors were outperformed in terms of their critical rotational rate. *Design II* with sloped winglets got the quadcopter to take off at just 5,400 rpm.

The test flights also allowed conclusions to be drawn about the electrodynamic properties of the rotors. To keep the Mavic Pro hovering, the motors had to generate 118 watts of electrical power for *Design II* with sloped winglets. This compares to just 110 watts for the DJI-standard rotors. The custom-designed rotors were thus less energy efficient. In addition to manufacturing and material reasons, aerodynamic factors such as the glide ratio may have also contributed to this.

The initial goal of the paper was by far surpassed. A prototype was successfully produced that outperformed the lift performance characteristics of the industrially produced rotors of the world market leader DJI. In any follow-up projects, it will be of particular interest to focus on material aspects. The test flights have shown the great influence of the material used, the manufacturing processes applied and the surface quality on the aerodynamic performance of the rotor.

8. List of sources

[1]   https://de.wikipedia.org/wiki/Kutta-Schukowski-Transformation

        (last visited on 23. August 2020)

[2]   https://www.badische-zeitung.de/biologische-schaedlingsbekaempfung-mit-drohnen-hat-sich-etabliert--187412685.html

        (last visited on 02. September 2020)

[3]   https://www.thphys.uni-heidelberg.de/~huefner/PhysikUeberall/V07S.pdf

        (last visited on 22. February 2019)

[4]   Gasch R. Auslegung von Windturbinen nach Betz und Schmitz. *Windkraftanlagen* 2005: S. 179-216

[5]   https://de.wikipedia.org/wiki/Str%C3%B6mungswiderstand

        (last visited on 23. August 2020)

[6]   https://www.spektrum.de/lexikon/mathematik/induzierter-widerstand-der-aerodynamik/4363

        (last visited on 24. February 2019)

[7]   https://www.boldmethod.com/learn-to-fly/aerodynamics/how-winglets-work-to-reduce-drag-and-how-wingtip-vortices-form/

        (last visited on 23. August 2020)

[8]   http://airfoiltools.com/search/list?page=a&no=0

        (last visited on 22. August 2020)

[9]   Herwig H. Strömungsphänomene. *Strömungsmechanik* 2008: S. 20-26

[10]   Daude M. *Winglets for Aircraft Wing Tips*. U.S. Patent 4'457'479

[11]   RWTH Aachen. Drehimpuls, Drehimpulssatz und Drehimpulserhaltungssatz. Vorlesungsbegleitende Unterlagen 2018: *Mechanik II Dynamik*:79-85

【評語】100044

This work is aimed to design and fabricate a rotor that would allow a quadcopter to hover flight. The author comes up with Design II with slopped winglets to achieve lift performance better than a standard rotor. The project is conducted with a properly constructed experiment hardware and the simulation for the calculation is well-organized. However, the surface roughness of the printed rotor should be considered, especially for the discussion of aerodynamics in the airflow. In addition, the criteria for choosing the shape of airfoil can be emhasized.